Identification of a stereotypic molecular arrangement of endogenous glycine receptors at spinal cord synapses

Stephanie A Maynard[1], Philippe Rostaing[1], Natascha Schaefer[2], Olivier Gemin[1], Adrien Candat[1], Andréa Dumoulin[1], Carmen Villmann[2], Antoine Triller[1]*, Christian G Specht[1,3]*

[1] Institut de Biologie de l'ENS (IBENS), Ecole Normale Supérieure, CNRS, Inserm, Université PSL, Paris, France

[2] Institute for Clinical Neurobiology, University Hospital, Julius-Maximilians-University, Würzburg, Germany

[3] Diseases and Hormones of the Nervous System (DHNS), Inserm, Université Paris-Saclay, Le Kremlin-Bicêtre, Paris, France

* correspondence: christian.specht@inserm.fr, triller@biologie.ens.fr

ORCID numbers:

Stephanie A Maynard 0000-0002-7838-3676

Natascha Schaefer 0000-0001-9743-1963

Olivier Gemin 0000-0003-3210-7876

Andréa Dumoulin 0000-0003-1309-3448

Carmen Villmann 0000-0003-1498-6950

Antoine Triller 0000-0002-7530-1233

Christian G Specht 0000-0001-6038-7735

Short title:

Quantitative SR-CLEM of glycinergic synapses

Key words

single molecule localization microscopy (SMLM); glycine receptor (GlyR); gephyrin; photoactivated localization microscopy (PALM); correlative light and electron microscopy (CLEM); super-resolution CLEM (SR-CLEM); super-resolution radial fluctuation (SRRF) analysis; spinal cord; synapse; hyperekplexia; oscillator mouse model; hypomorph

1

34 **Abstract**

35 Precise quantitative information about the molecular architecture of synapses is essential to

36 understanding the functional specificity and downstream signaling processes at specific

37 populations of synapses. Glycine receptors (GlyRs) are the primary fast inhibitory

38 neurotransmitter receptors in the spinal cord and brainstem. These inhibitory glycinergic

39 networks crucially regulate motor and sensory processes. Thus far the nanoscale organization

40 of GlyRs underlying the different network specificities has not been defined. Here, we have

41 quantitatively characterized the molecular arrangement and ultra-structure of glycinergic

42 synapses in spinal cord tissue using quantitative super-resolution correlative light and electron

43 microscopy (SR-CLEM). We show that endogenous GlyRs exhibit equal receptor-scaffold

44 occupancy and constant packing densities of about 2000 GlyRs μm^{-2} at synapses across the

45 spinal cord and throughout adulthood, even though ventral horn synapses have twice the total

46 copy numbers, larger postsynaptic domains and more convoluted morphologies than dorsal

47 horn synapses. We demonstrate that this stereotypic molecular arrangement is maintained at

48 glycinergic synapses in the *oscillator* mouse model of the neuromotor disease hyperekplexia

49 despite a decrease in synapse size, indicating that the molecular organization of GlyRs is

50 preserved in this hypomorph. We thus conclude that the morphology and size of inhibitory

51 postsynaptic specializations rather than differences in GlyR packing determine the

52 postsynaptic strength of glycinergic neurotransmission in motor and sensory spinal cord

53 networks.

54

55 **Introduction**

56 Synaptic transmission relies on the integration of spatially and temporally controlled signals

57 by neurotransmitter receptors in the postsynaptic membrane. The molecular arrangement of

58 postsynaptic receptors and scaffold proteins is therefore key to the synaptic function, however

59 the heterogeneity and complexity of postsynaptic sites has made it difficult to resolve its

60 internal organization, to ascertain whether distinct compositional states exist, and to

61 determine how the organization is affected in disease.

62

63 Glycine receptors (GlyRs) are the main inhibitory neurotransmitter receptors in the adult

64 spinal cord and brainstem. Glycinergic neurons arise from different embryonic origins, with

65 specific types of neurons residing in characteristic layers of the spinal cord (Lu et al., 2015).

66 Depending on their location, glycinergic neurons mediate sensory and motor information in

67 the dorsal and ventral spinal cord, respectively, which requires high reliability and fidelity of

2

68 transmission (Alvarez, 2017). Consequently, deficits in glycinergic transmission are involved

69 in pain mechanisms (Harvey et al., 2004) and motor-related neurological diseases (Schaefer et

70 al., 2018). The electrophysiological properties of glycinergic currents indicate that only a

71 limited number of receptors are activated by the release of a single synaptic vesicle

72 (Oleskevich et al., 1999, Singer & Berger, 1999), suggesting that the nanoscale organization

73 of the receptors determines signal amplitude.

74

75 It has been shown that neurotransmitter receptors at excitatory and inhibitory synapses are

76 organized within sub-synaptic domains (SSDs) that are aligned with presynaptic elements of

77 the active zone (AZ) (Crosby et al., 2019, MacGillavry et al., 2013, Pennacchietti et al., 2017,

78 Tang et al., 2016, Yang et al., 2021). These so-called trans-synaptic nanocolumns are thought

79 to increase the efficacy of synaptic transmission (Haas et al., 2018). At mixed inhibitory

80 synapses, both glycine and $GABA_A$ receptors are immobilized opposite to presynaptic release

81 sites through direct interactions with their common scaffold protein gephyrin (Maric et al.,

82 2011, Specht et al., 2013, Yang et al., 2021). However, accurate quantification of receptor

83 numbers and their precise arrangement within postsynaptic sites in native tissue is lacking.

84 Further, the question is raised as to whether the structure of glycinergic synapses varies in

85 functionally diverse circuits of the dorsal and ventral spinal cord, if it changes over time, and

86 if it is disturbed in GlyR pathologies such as the neuromotor disease hyperekplexia in

87 humans. In hyperekplexic patients, mutations in the receptor subunit genes *GLRA1* and *GLRB*

88 lead to decreased receptor availability and disturbances in glycinergic transmission, resulting

89 in exaggerated startle reflexes, muscle hypertonia and stiffness in infancy (Chung et al., 2013,

90 Chung et al., 2010, Schaefer et al., 2013).

91

92 To investigate whether the molecular arrangement of GlyRs may account for differences in

93 the functional specificity of sensory and motor circuits we have quantitatively analyzed the

94 ultra-structural organization of inhibitory synapses in spinal cord tissue. We have combined

95 molecule counting of endogenous GlyRs using single molecule localization microscopy

96 (SMLM) with correlative light and electron microscopic analysis (CLEM) to obtain receptor

97 numbers as well as detailed spatial information of the synapse at the nanometer scale. We

98 have further examined to what extent the molecular organization is maintained throughout

99 adult development and during GlyRα1-deficiency. We show that GlyRs are packed at a

100 constant density of about 2000 receptor complexes per μm^2 at mature synapses, suggesting

101 that they are assembled in a stereotypic fashion. This GlyR molecular organization is

102   maintained in the hyperekplexia model *oscillator* despite a decrease in ventral synapse size,

103   indicating that GlyRα1-deficiency does not affect the integrity of the synaptic arrangement as

104   such. Collectively, our results provide the structural basis for understanding the mechanisms

105   underlying receptor availability and the integration of neurotransmitter-induced signals.

106

107   **Results**

108   **Generation of a KI model expressing endogenous levels of mEos4b-GlyRβ**

109   In order to quantify GlyR numbers and their precise distribution at synapses we generated a

110   knock-in (KI) mouse model expressing endogenous mEos4b-tagged GlyRβ subunits (Fig. S1).

111   The β-subunit drives the synaptic localization of the receptor through direct interactions with

112   the synaptic scaffold protein gephyrin at inhibitory synapses (Kim et al., 2006, Meyer et al.,

113   1995). To date, labeling of GlyRβ *in situ* using immunocytochemistry has proven difficult

114   due to a lack of reliable antibodies that recognize the native β-subunit (only antibodies for

115   Western blotting recognizing the denatured protein are available), which has severely limited

116   the study of the receptor. The coding sequence of mEos4b was inserted in exon 2 of the *Glrb*

117   gene by homologous recombination supported by a guide RNA (CRISPR-Cas9) to increase

118   recombination efficiency (ICS, Illkirch, France). Specifically, the fluorophore sequence was

119   inserted after the signal peptide and before the N-terminus of the mature GlyRβ subunit,

120   meaning that it does not interrupt the coding sequence of the receptor (Fig. S1B). The correct

121   insertion was confirmed by amplification and sequencing of genomic DNA. Semi-quantitative

122   RT-PCR revealed that equal concentrations of $Glrb^{Eos}$ and the wild-type transcript ($Glrb^{WT}$)

123   are expressed in heterozygous animals. When bred to homozygosity, KI animals follow

124   Mendelian inheritance (Fig. S2A), exhibit normal lifespans (Fig. S2B), and display no overt

125   phenotype, suggesting that the GlyR expression and/or function are not altered.

126

127   To further confirm that GlyR function is not altered by the introduction of mEos4b, we

128   carried out whole cell recordings in cultured spinal cord neurons of $Glrb^{WT/WT}$ and

129   homozygous $Glrb^{Eos/Eos}$ animals (Fig. S2C). The agonist glycine was applied in a

130   concentration series from 1 μM to 300 μM. The maximal chloride currents at saturating

131   glycine concentrations of 300 μM were not significantly different in $Glrb^{Eos/Eos}$ animals,

132   despite a minor increase in the EC_{50} ($Glrb^{WT/WT}$ 100 ± 5 μM, $Glrb^{Eos/Eos}$ 130 ± 9 μM, p =

133   0.0123 t-test). In view of the millimolar concentration of glycine present during synaptic

134   transmission (Beato, 2008, Legendre, 1998) these data indicate that the presence of the N-

4

135   terminal fluorophore does not affect GlyR function under physiological conditions. Hill

136   coefficients for $Glrb^{\text{WT/WT}}$ and $Glrb^{\text{Eos/Eos}}$ were in a range of 3.5-4, arguing for cooperativity

137   of the subunits during glycine binding. The glycinergic origin of the chloride influx was

138   confirmed by blocking the currents recorded in the presence of 100 μM glycine with 10 μM

139   strychnine.

140

141   **Quantitative confocal imaging of endogenous mEos4b-GlyRβ and mRFP-gephyrin at**

142   **spinal cord synapses in tissue**

143   To verify the expression and synaptic targeting of the mEos4b-GlyRβ protein we carried out

144   quantitative confocal imaging in 40 μm vibratome tissue sections. $Glrb^{\text{Eos/Eos}}$ animals were

145   crossed with a previously established KI mouse line expressing mRFP-tagged gephyrin to

146   visualize inhibitory postsynaptic sites (Specht et al., 2013). Since the synaptic localization of

147   the GlyR is strictly dependent on its interaction with gephyrin (Patrizio et al., 2017), we

148   expected a high degree of co-localization of the two proteins in the brainstem and spinal cord

149   (Zeilhofer et al., 2005). Indeed, mEos4b-GlyRβ was widely expressed at inhibitory synapses

150   in the thalamus, midbrain, pons and medulla (Fig. S3). Very little fluorescence was detected

151   in the forebrain despite the high reported expression of the *Glrb* transcript (Fujita et al., 1991,

152   Malosio et al., 1991), suggesting that protein levels are controlled by post-transcriptional

153   mechanisms in a region-specific manner, as previously proposed (Weltzien et al., 2012).

154

155   In the spinal cord, we observed bright punctate mEos4b-GlyRβ signals throughout the gray

156   matter, with the exception of the superficial laminae of the dorsal horn, where the intensity of

157   the green fluorescence was markedly lower (Fig. 1A). The expression of mEos4b-GlyRβ and

158   mRFP-gephyrin in homozygous and heterozygous animals was quantified in confocal images

159   of thoracic and lumbar spinal cord slices at 2 months (Fig. 1B) and 10 months of age (Fig. S4).

160   The same region of the ventral horn, indicated by the white square in Fig. 1A was taken for

161   quantification of mEos4b-GlyRβ and mRFP-gephyrin expression in all conditions. The

162   integrated mEos4b intensity at gephyrin-positive ventral horn synapses was exactly two times

163   higher in $Glrb^{\text{Eos/Eos}}$ mice than in $Glrb^{\text{Eos/WT}}$, demonstrating that both alleles are expressed

164   with the same efficiency, and that the mEos4b fluorophore does not affect the synaptic

165   localization of the receptor complexes. To confirm that the confocal image acquisition was in

166   the linear dynamic range we bleached the mEos4b fluorophores by repeatedly scanning the

5

167 same tissue area at constant laser power (Fig. 1A, white square), which resulted in a linear

168 decay of pixel intensities over a range of more than 20 fold (Fig. 1C).

169

170 Across the spinal cord slices, the intensity of synaptic mEos4b-GlyRβ puncta increased from

171 dorsal to ventral both in homozygous (Fig. 1D-E) and in heterozygous animals (Fig. S4).

172 Similarly, mRFP-gephyrin fluorescence was higher and more variable in the ventral horn,

173 suggesting that synapses were on average about twice as big as those in the dorsal horn,

174 despite being fewer in number (Fig. 1F, S4). The mEos4b/mRFP ratio was relatively equal

175 across the spinal cord with the exception of the superficial layers of the dorsal horn, where

176 GlyR levels were largely exceeded by gephyrin (Fig. 1A and D). The lower GlyR-scaffold

177 occupancy of synapses in laminae I-III can be explained by the predominant expression of

178 $GABA_A$Rs that compete for receptor binding sites at these mixed inhibitory synapses

179 (Alvarez et al., 1996, Lorenzo et al., 2014, Todd et al., 1996).

180

181 **Dual-color super-resolution imaging of glycinergic spinal cord synapses**

182 To quantify the observed structural differences at super-resolution, we combined radial

183 fluctuation (SRRF) analysis of mRFP-gephyrin and photo-activated localization microscopy

184 (PALM, a form of SMLM) of mEos4b-GlyRβ in spinal cord tissue from double KI animals.

185 Sucrose impregnated cryosections of 2 μm thickness were prepared from dorsal and ventral

186 tissue and placed on gridded coverslips (Fig. 2A). SRRF and PALM images were acquired

187 sequentially. First, mRFP signals were recorded with high intensity 561 nm laser illumination

188 until all mRFP fluorophores were bleached (10,000 frames). mEos4b was then

189 photoconverted with increasing 405 nm laser intensity and imaged at 561 nm for 25,000

190 frames until all available fluorophores were exhausted. By acquiring both fluorophores,

191 mRFP and photoconverted mEos4b, in the same emission band (607/36 nm), any chromatic

192 misalignment between the two super-resolved images was eliminated. SRRF reconstruction

193 was carried out on the raw mRFP image sequence and PALM images were generated from

194 individual mEos4b detections using Gaussian peak fitting (Fig. 2B). The spatial resolution

195 was estimated using Fourier ring correlation (FRC), which measures the similarity of two

196 images as a function of spatial frequency by comparing the odd and even frames of the raw

197 image sequence. According to this analysis, the spatial resolution of SRRF was 46 nm and

198 that of PALM 21 nm. It should be noted that the synaptic puncta in the SRRF images appear

199 somewhat smaller and brighter due to differences in the reconstruction methods that result in

200 differences in the dynamic intensity range.

201

202 The majority of synaptic clusters in the dual super-resolution images were small and spherical

203 or elongated. Larger clusters displayed a variety of morphologies including elongated shapes

204 seen in side-view (Fig. 2B) as well as convoluted structures, and were more frequently

205 observed in the ventral horn (Fig. S5). All mEos4b-GlyR clusters closely matched the mRFP-

206 gephyrin clusters, confirming the localization of the receptors in the postsynaptic membrane.

207 As expected of two directly interacting synaptic components the degree of co-localization of

208 mEos4b-GlyRβ and mRFP-gephyrin was very high, with mean intensity correlation quotients

209 (ICQ) around 0.3 (Fig. 2C and S5), a value indicative of close spatial correlation (Li et al.,

210 2004). Minor mismatches between the super-resolution images are explained by the fact that

211 the majority of synapses are seen in cross-section and that the two fluorophores are located on

212 opposite sides of the postsynaptic membrane (~30 nm distance, (Specht et al., 2013)). There

213 were no obvious differences between the ICQ values of dorsal versus ventral synapses (0.28-

214 0.3), indicating equivalent GlyRβ-gephyrin binding in the two regions. It should be noted that

215 the ICQ reflects relative fluctuations between images and is not sensitive to absolute

216 differences in signal intensities, resulting in similar ICQ values in animals that are

217 heterozygous or homozygous for mRFP-gephyrin (Fig. 2C). Quantitative comparison of

218 mEos4b-GlyRβ and mRFP-gephyrin intensities confirmed that the amounts of receptor and

219 scaffold proteins are closely correlated, and that the occupancy of receptor binding sites is the

220 same in the dorsal and ventral horn, independent of synapse size (Fig. 2D and S5). To

221 estimate the sizes of the synapses we applied a density threshold to the PALM pointillist

222 images and calculated the areas of the mEos4b-GlyRβ clusters (Fig. 2E). The mean synapse

223 area in the ventral horn was larger and more variable than in the dorsal region, both in animals

224 of 2 and 10 months of age (Fig. 2F). We also remarked that the overall number of synapses in

225 ventral horn tissue was lower compared to the dorsal horn, significantly so by 10 months (Fig.

226 2G, see also Fig. 1F and S4). The inverse relationship between synapse number and size is

227 likely due to the presence of different cell types in the two regions, specifically Renshaw cells

228 and large motor neurons in the ventral horn that require strong inhibitory control (e.g.

229 (Bhumbra et al., 2014)).

230

231 **Quantification of GlyR numbers and densities at native spinal cord synapses**

232 Given that mEos4b-GlyRβ subunits are expressed at endogenous levels in $Glrb^{Eos/Eos}$ animals

233 and that all the fluorophores were exhausted during the PALM recordings, we were able to

234 count the number of GlyRs at spinal cord synapses. The total number of mEos4b-GlyRβ

235 detections at synapses (Fig. S6) were converted into molecule numbers taking into account

236 the blinking properties of the fluorophore and the α_3:β_2 stoichiometry of the pentameric GlyR

237 complex (Durisic et al., 2014, Patrizio et al., 2017). To this aim, the average number of

238 detections per fluorophore (detections/burst) and the fraction of functional fluorophores

239 (probability of detection, P_{det}; Fig. S7) were determined in each set of experiments using

240 extrasynaptic receptor complexes (Fig. 2E, red arrowheads). We calculated a median copy

241 number of 114 pentameric GlyR complexes at dorsal horn synapses and twice that number at

242 ventral horn synapses in 2 month old animals (Fig. 2H). Copy numbers were almost identical

243 at 10 months (Fig. S8), indicating that the glycinergic network was mature at both time points.

244 These numbers exceed estimates derived from electrophysiological recordings in new-born,

245 juvenile and adult rat spinal cord neurons that suggest the activation of as few as 7 and up to

246 about 110 GlyRs during an average miniature inhibitory postsynaptic current (mIPSC) (Chery

247 & de Koninck, 1999, Oleskevich et al., 1999, Singer & Berger, 1999, Takahashi, 1992). The

248 high numbers of GlyRs measured by fluorophore counting therefore imply that the available

249 receptors are not saturated by quantal release, which is likely to increase the dynamic range of

250 postsynaptic inhibition (Alvarez, 2017).

251

252 Our quantitative PALM data further demonstrate that differences in receptor numbers result

253 from differences in synapse size (Fig. 2F). By combining the two parameters, we derived

254 mean GlyR densities of ~2000 μm^{-2} (Fig. 2I, S8). Similar receptor densities of 1250 μm^{-2} and

255 ~2000 μm^{-2} have been measured at GABAergic synapses in cerebellar stellate cells and in

256 cultured hippocampal neurons, respectively (Liu et al., 2020, Nusser et al., 1997). We saw no

257 differences in the GlyR packing density at dorsal and ventral horn synapses, nor did we find a

258 clear size dependence, as determined by linear regression of all synapses (Fig. 2I) and the

259 evolution of the coefficient of variation of GlyR density with respect to synapse area (Fig. S8).

260 These findings are significant because they indicate that GlyR density is constant and largely

261 independent of neuron type, embryonic origin or physiological function. Assuming that

262 gephyrin molecules are clustered at densities of up to 9000 μm^{-2} (Specht et al., 2013), our data

263 also suggest that close to 50% of the receptor binding sites are occupied by GlyRs at native

264 spinal cord synapses, in line with earlier observations of GlyR subunits that were

265 overexpressed in cultured neurons (Patrizio et al., 2017).

266

267

8

Quantitative SR-CLEM of GlyRβ molecular organization

To integrate the results of molecule counting with three-dimensional ultra-structural information and the exact synapse size, we further analyzed dorsal and ventral horn synapses by SR-CLEM. Previously imaged cryosections of $Glrb^{Eos/Eos}$ tissue from 10 month old animals were embedded in epoxy resin, and ultra-thin (70 nm) serial sections were collected on EM slot grids with an ultramicrotome (Fig. 3A). After osmium tetroxide enhancement, electron micrographs of identified synapses were acquired in all serial sections and registered manually, using the coverslip grids and cellular structures as reference (Fig. 3B-C). All of the synapses that were both, imaged by PALM and reconstructed with EM were functionally mature, as judged by the apposition of a single presynaptic terminal containing synaptic vesicles. In line with our PALM data we found that glycinergic synapses in the ventral horn were substantially larger and more variable in size than those in the dorsal horn (Fig. 3C-D). There was good correspondence between the calculated synapse areas in the EM and PALM image reconstructions, even though PALM underestimated the sizes of some large ventral horn synapses (Fig. S9). This is probably due to the fact that a majority of synapses are tilted, and that the axial component of the area is not captured in the SMLM projections. Whereas most synapses in the dorsal horn were macular, ventral synapses were frequently composed of sub-domains (Fig. 3E-G). In agreement with earlier studies (Alvarez et al., 1997, Lushnikova et al., 2011, Santuy et al., 2018), the degree of complexity scales with the size of the postsynaptic specialization (Fig. 3F), and was taken into account for the calculation of the combined area in the EM serial sections.

The ratio of GlyR copy numbers and the area of the inhibitory postsynaptic specialization obtained by EM resulted in average receptor densities of approximately 2000 μm^{-2} (Fig. 3H). Consistent with our PALM estimates we did not observe significant differences between synapses in the dorsal and the ventral horn (Fig. 2I, S8). Furthermore, the GlyR packing density was not dependent on synapse size (Fig. 3I), supporting an earlier proposal (Lim et al., 1999). This suggests that GlyRs are assembled in a systematic manner, where receptor numbers increase linearly with synapse size. Since the morphological complexity of synapses increases with size, it can also be concluded that GlyR occupancy at individual sub-domains of the postsynaptic sites is uniform. GlyR densities were indeed not significantly different within sub-clusters of reconstructed synapses (Fig. 3G and I, black data points). Together, these findings point to a tight regulation of the architecture of glycinergic synapses across different molecular length scales, where GlyRs are arranged in sub-synaptic signaling units.

9

302

GlyR packing density is unaltered in the hyperekplexia mouse model *oscillator*

Having identified that GlyRs have a stereotypic molecular organization that is maintained throughout adulthood and across synapses in different neuronal circuits, we questioned whether this arrangement is altered in a mouse model of hyperekplexia, a motor-related neurological disease that significantly impacts motor processing in the ventral horn of the spinal cord. The mouse mutation *oscillator (Glra1$^{\text{spd-ot/spd-ot}}$)* is recessively inherited and causes a microdeletion and frameshift in the TM3-4 intracellular loop of the GlyRα1 subunit leading to subunit truncation and subsequent loss of functional GlyRs at synapses (Kling et al., 1997). Homozygous *oscillator* mice do not live past 3 weeks of age (Buckwalter et al., 1994). In contrast, heterozygous animals have a normal lifespan and exhibit a more subtle phenotype. *Glra1*$^{\text{spd-ot/WT}}$ mice display an increased startle reflex and lower GlyRα1 levels (Kling et al., 1997), making them a suitable model for human hyperekplexia. We generated mutant mice that were homozygous for mEos4b-GlyRβ (as described above) and heterozygous for *oscillator* (*Glrb*$^{\text{Eos/Eos}}$ / *Glra1*$^{\text{spd-ot/WT}}$) as well as wild-type (WT) littermates (*Glrb*$^{\text{Eos/Eos}}$ / *Glra1*$^{\text{WT/WT}}$). In these experiments, inhibitory synapses were detected by immunolabeling of endogenous gephyrin using the mAb7a antibody.

Quantitative confocal imaging in 40 μm vibratome tissue sections showed bright punctate mEos4b-GlyRβ signals localized at synapses (Fig.4A). Across the spinal cord slices, the intensity of synaptic mEos4b-GlyRβ puncta increased from dorsal to ventral in wild-type animals (Fig. 4B), replicating the intensity profile observed previously (Fig. 1D). The intensity of synaptic mEos4b-GlyRβ puncta in heterozygous *oscillator* animals were substantially lower than those of WT littermates, which explains the reductions in membrane levels of GlyR and gephyrin previously observed by Western blotting (Kling et al., 1997). The mEos4b/gephyrin-7a ratio was relatively equal across the spinal cord with greater variation seen in *oscillator*. No ectopic GlyRβ clusters were detected, meaning that GlyRs and gephyrin always colocalized (Fig. S10). The number of gephyrin-positive synapses across the spinal cord remained unchanged between WT and *oscillator*.

Using our quantitative PALM approach, we determined the number and size of glycinergic synapses in tissue slices of dorsal and ventral spinal cord, as well as the mEos4b detection density (Fig S11), in order to understand the alterations in glycinergic synapse architecture in

10

335   this mutant mouse model. The detections per synapse were converted into molecule numbers

336   as described before (Fig. S7 and S12). In WT animals we observed small and spherical dorsal

337   synapses and larger, elongated ventral synapses, while *oscillator* synapses appeared small

338   both in dorsal and ventral horn tissue (Fig. 5A). This was confirmed by quantitative analysis.

339   The mean synapse area in the ventral horn was significantly larger than in the dorsal region in

340   WT animals (Fig. 5B), in agreement with our earlier data (Fig. 2F). However, this difference

341   was lost in *Glra1*$^{\text{spd-ot/WT}}$ littermates. The overall number of synapses was lower in ventral

342   horn tissue compared to the dorsal horn in both WT and *oscillator* animals (Fig. 5C). These

343   data suggest that the decrease in functional receptors in heterozygous *oscillator* mice

344   manifests itself as a reduction in the size of ventral synapses.

345

346   We further quantified the total number of endogenous GlyRs at synapses (Fig. 5D) and found

347   that the number and distribution of receptors in WT mice matched that of 2 and 10 month old

348   WT animals analyzed previously (Fig. 2H and S8). This is remarkable considering that these

349   experiments were performed independently and subsequent to the previous dataset, attesting

350   to the stability of the measurements. It should also be pointed out that the GlyR copy numbers

351   were indistinguishable from those in mRFP-gephyrin double KI animals, confirming that the

352   presence of the fluorophores does not affect their expression and synaptic clustering. We

353   found similar copy numbers in dorsal synapses of heterozygous *oscillator* mice compared to

354   WT littermates, however in ventral tissue we found a shift towards lower receptor numbers

355   per synapse, suggestive of smaller synapses. By combining the measurements of GlyR copy

356   numbers with synapse area we could derive the receptor density. Consistent with our previous

357   PALM data, we found a constant receptor density independent of synapse size in WT mice, as

358   judged by the shallow slope of the linear regression (Fig. 5E). We observed a similar and

359   constant GlyR packing density in synapses of *oscillator* mice. This suggests that despite a

360   decrease in the total number of functional GlyRs in the heterozygous *oscillator* mouse model

361   the molecular organization underlying receptor clustering within the synapse is maintained, in

362   line with the lack of an overt neuromotor phenotype in these animals. In other words, the

363   receptors are assembled stereotypically in the disease model, as in WT, with synapse size

364   consistently scaling with receptor number. Together, our findings describe a highly regulated

365   architecture of glycinergic synapses in both wild-type animals as well as in a model of

366   synaptic pathology, providing a structural basis of glycinergic signaling.

367

368

11

Discussion

Combining single molecule PALM imaging, molecular counting and 3D electron microscopy we have shown that glycinergic synapses in different regions of the spinal cord follow the same structural principle, insofar as their receptor-scaffold occupancy and packing densities are the same. This uniformity extends to the sub-synaptic level. The presence of so-called sub-synaptic domains (SSDs) at inhibitory synapses has been shown by super-resolution microscopy (Crosby et al., 2019, Dzyubenko et al., 2016, Pennacchietti et al., 2017, Specht et al., 2013, Yang et al., 2021). However, it remains controversial whether the identified patterns represent the overall structure of the postsynaptic specialization itself or whether they reflect intra-synaptic variations in molecule clustering. Our quantitative SR-CLEM data lend support to the first model, whereby inhibitory postsynaptic sites in the spinal cord are composed of sub-domains that determine the distribution of the GlyRs. This organization is achieved through direct interactions between GlyRs and gephyrin, as shown by the close correspondence between the receptors and scaffold proteins. As such, the GlyR sub-clusters at spinal cord synapses do not constitute SSDs within the postsynaptic membrane in the strict sense, since they exhibit uniform binding to the synaptic scaffold (discussed in (Yang & Specht, 2019)). The stereotypic GlyR density within SSDs observed in our study supports the idea that these structures can instead be equated with the convolutions of the synaptic junction observed by EM (Alvarez et al., 1997, Lushnikova et al., 2011, Peters & Palay, 1996, Santuy et al., 2018). The formation of these convolutions is probably a consequence of gephyrin oligomerization that appears to introduce an asymmetry in the synaptic scaffold. The situation may be different at GABAergic synapses, where the co-existence of gephyrin-dependent and gephyrin-independent clustering mechanisms could lead to the formation of spatially more restricted SSDs containing different $GABA_AR$ subtypes (Pennacchietti et al., 2017, Specht, 2020).

The nanoscale organization of inhibitory synapses is the same in glycinergic neurons in the dorsal and the ventral spinal cord, despite their different embryonic origins. Ventral horn synapses are generally larger, more complex and contain more GlyRs, suggesting that the size of the synapse is differentially regulated in a regional and cell type specific manner to adjust the level of glycinergic inhibition. As such, these synapses may be particularly well adapted to motor circuits, assuring strong and reliable inhibition of the postsynaptic neuron (Alvarez, 2017). At the same time, the long and tortuous perimeter of the postsynaptic specialization is likely to accelerate the dynamic exchange of GlyRs and other synaptic components (Chow et

12

403   al., 2017, Santuy et al., 2018), thereby promoting the molecular plasticity at complex

404   inhibitory synapses (Specht, 2020). Whether glycinergic plasticity results from transient

405   changes in GlyR occupancy and/or from the recruitment of extrasynaptic GlyR-gephyrin

406   complexes (Chapdelaine et al., 2021) has not been proven thus far. However, our data suggest

407   that ultimately it is the size and complexity rather than the GlyR packing density that is

408   dynamically regulated. It can further be argued that large and morphologically complex

409   synapses may be particularly well adapted to integrate fast repetitive, or indeed multi-

410   vesicular release arising from one or more presynaptic sites, thus providing a strong and

411   reliable inhibition of the postsynaptic neuron while maintaining fast neurotransmitter

412   clearance (discussed in (Alvarez, 2017, Rudolph et al., 2015)).

413

414   In addition, our data show that GlyR density and occupancy do not change between 2 and 10

415   months of age, indicating that receptor clustering is fully mature by the earlier time point.

416   Studies of normal aging of spinal cord synapses are scarce, and its effect on receptor

417   organization has not been studied. Broadhead and colleagues (Broadhead et al., 2020) report

418   no difference between the number of excitatory synapses in the ventral horn and only a slight

419   increase in dorsal synapses between 2 to 9 month old mice. Broadly in line with these

420   findings, we found no difference in the number of synapses, synapse area, and GlyR packing

421   density in dorsal and ventral tissue between 2 and 10 months. Thus, glycinergic postsynaptic

422   sites show considerable control over their molecular composition throughout adulthood,

423   further emphasizing the functional significance of their synaptic architecture in both sensory

424   and motor signaling. Our data therefore suggest that a constant GlyR density potentially

425   provides the most efficient organization of the glycinergic postsynaptic site, while enabling

426   the refinement of the size and complexity of the synapse due to ongoing neural activity.

427

428   Their molecular organization sets glycinergic synapses apart from excitatory synapses that do

429   not exhibit systematic receptor clustering. Different glutamate receptors are highly variable

430   and occupy separate sub-synaptic domains within the overall postsynaptic density (PSD)

431   (Goncalves et al., 2020). The number of AMPARs at excitatory synapses can range from

432   essentially zero (at silent synapses) to more than 100 (Nusser et al., 1998). Within SSDs, the

433   average AMPAR density has been estimated at around 5000 μm^{-2} (Goncalves et al., 2020),

434   although the absolute values will have to be confirmed using quantitative labeling strategies

435   such as the one described here. Interestingly, AMPAR content of SSDs was shown to vary in

436   response to synaptic plasticity without an apparent change in SSD size (Compans et al.,

13

437   2021). This suggests that the packing density of AMPARs is not constant even at the

438   nanoscale, which may be the basis for AMPAR plasticity at excitatory synapses.

439

440   The neuromotor disease hyperekplexia results from defects in glycinergic inhibition in

441   humans. Several mouse models with analogous mutations in the *Glra1* gene recapitulate the

442   phenotype of exaggerated startle reflexes and muscle stiffness (Schaefer et al., 2018). In

443   general, the mutations in the various mouse models are less well tolerated than in humans and

444   often have lethal phenotypes in homozygotes. Hyperekplexia can be recessively or

445   dominantly inherited in humans, but neither has been shown to cause lethality. The *oscillator*

446   mouse model, whilst lethal in the homozygous form, displays a relatively mild phenotype in

447   heterozygous animals, with a measurable startle reflex and normal lifespan (Kling et al.,

448   1997). Heterozygous *oscillator* therefore represents a relevant model for the subtler

449   phenotype in humans and the long-term stability of glycinergic synapses beyond the

450   developmental stage at which lethality occurs in homozygous animals. However, it is not

451   known how the reduced GlyR levels in the *Glra1*$^{\text{spd-ot/WT}}$ hypomorph can affect (and sustain)

452   functional motor networks. Our characterization of the molecular organization of

453   heterozygous *oscillator* synapses shows that GlyR packing follows the same principle as in

454   wild-type synapses, even though the total number of available functional receptors is reduced,

455   resulting in smaller synapses in the ventral spinal cord. This further emphasizes that the

456   stereotypic arrangement of GlyRs dictates the size of the postsynaptic domain. Most of the

457   synapses that are formed in heterozygous *oscillator* likely achieve a size threshold capable of

458   sustaining glycinergic signaling without serious motor defects. The lack of fundamental

459   structural changes at glycinergic synapses further suggests that no or only limited

460   compensatory effects take place in *oscillator*, in agreement with earlier findings that α1β

461   heteropentameric GlyR complexes cannot be compensated for by other subunit

462   configurations, α1-homopentamers or GABA$_A$Rs (Schaefer et al., 2012). Our findings thus

463   provide a new perspective into the molecular basis of GlyRα1-deficiency in an animal model

464   of human hyperekplexia.

465

466   Taken together, our data show that dorsal and ventral synapses are distinct populations.

467   Ventral horn synapses have much higher GlyR copy numbers, even though receptor density is

468   not different. In contrast to the relatively compact, macular synapses in the dorsal horn,

469   ventral horn synapses achieve a greater receptor number by enlarging the synaptic surface,

14

470   thus multiplying the sites of signal transmission. These region-specific glycinergic synapse

471   morphologies are likely to underlie functional differences at sensory (dorsal) versus motor

472   (ventral) circuits.

473

474

475   **<u>Acknowledgements</u>**

487

488   **<u>Author contributions</u>**

489   SAM and CGS planned the experiments; SAM, PR, NS, OG, AC, AD, and CGS performed

490   the experiments; SAM, PR, NS, CV and CGS analyzed the data; CV generated the oscillator

491   strain; CV and AT secured funding; SAM and CGS wrote the manuscript; all authors read and

492   approved the manuscript.

493

494   **<u>Declaration of interests</u>**

495   The authors declare no competing interests.

496

497   **<u>Data and materials availability</u>**

498   All data are available upon request.

499

500

501

502

503

504 **Materials and Methods**

505 **KI mouse model generation**

506 The knock-in (KI) mouse line C57BL/6N-*Glrb*^{tm1Ics} (MGI:6331106) carrying the mutant allele

507 *Glrb*^{tm1(Eos4)Ics} (MGI:6331065) was created by homologous recombination at the Institut

508 Clinique de la Souris (ICS, Illkirch, France). Flanked by 5' and 3' homology arms of 1.23 kb

509 and 3.49 kb, respectively, the targeting vector encompassed exon 2 of the *Glrb* gene with an

510 insertion of the coding sequence of mEos4b, as well as a *floxed* neomycin selection cassette

511 containing the Cre recombinase under control of protamine promoter in intron 2-3. The

512 selection cassette was excised in the F1 generation by germline expression of Cre, resulting in

513 a single *loxP* site in intron 2-3 of the *Glrb* locus (Fig. S1A). The correct insertion of the

514 mEos4b coding sequence was confirmed by sequencing of genomic *Glrb*^{Eos/Eos} tail DNA.

515 Genotyping was done using three primers (primer 1: TACCTTCTTGTTTTCTCTCC; primer

516 2: GTCTGTTTTCCCTCATAAGG; primer 3: TCGCTTTTGTAAATGATATGG) for the

517 amplification of the mutant *Glrb*^{Eos} (243 bp product) and/or the wild-type alleles (404 bp).

518

519 Purified spinal cord mRNA of *Glrb*^{Eos/Eos}, *Glrb*^{Eos/WT} and *Glrb*^{WT/WT} animals was reverse

520 transcribed (primer 6: GGAGTCTAACAGTAATCTGG), and amplified (primer 4:

521 AGGCGCGTCAAACTCGG; primer 5: CCATACCAACCAATGAAAGG). The correct

522 splicing of the mutant transcript was confirmed by sequencing of amplified cDNA. For semi-

523 quantitative RT-PCR, the *Glrb*^{Eos/Eos} mRNA was spiked with wild-type cDNA at a ratio of

524 1:2, 1:1 and 2:1 and amplified (Fig. S1B).

525

526 All experiments (with the exception of the data in Fig. 4, 5, S1, S2, and S10-12) were carried

527 out with F2 animals resulting from a cross between the KI line C57BL/6N-*Glrb*^{tm1Ics} (see

528 above) and a KI mouse line expressing mRFP-tagged gephyrin (*Gphn*^{mRFP}) (Machado et al.,

529 2011) in the C57BL/6J strain, meaning that the mice had a mixed C57BL/6N x C57BL/6J

530 genetic background.

531

532 Adult *Glra1*^{spd-ot} mice (*oscillator*, JAX stock #000536) from Jackson Laboratories (Bar

533 Harbor, ME, USA) were transferred to the animal facility of the Institute of Clinical

534 Neurobiology (Würzburg, Germany). Genotyping was done using primer 7:

535 GCCTCCGTGCTTTCTCCCTGC and primer 8: CCAGCCACGCCCCAAAG for the

536 amplification of the mutant *Glra1*^{spt-ot} (187 bp product) and/or the wild-type alleles (194 bp).

537 *Oscillator* mice were backcrossed into the C57BL/6J background for at least 15 generations.

538   Heterozygous $Glrb^{Eos/WT}$ animals were crossed with heterozygous *oscillator* mice for two

539   generations giving rise to F2 heterozygous *oscillator* animals that are homozygous for the

540    $Glrb^{tm1(Eos4)Ics}$ allele ($Glra1^{+/spd-ot}/Glrb^{Eos/Eos}$). These animals had a mixed C57BL/6N x

541   C57BL/6J genetic background and were used for the experiments shown in Fig. 4, 5 and S10-

542   12.

543

544   All experiments were in accordance with European Union guidelines and approved by the

545   local veterinary authorities. Animals at IBENS were treated in accordance with the guidelines

546   of the French Ministry of Agriculture and Direction Départementale des Services Vétérinaires

547   de Paris (École Normale Supérieure, Animalerie des Rongeurs, license B 75-05-20).

548   Procedures carried out at the Institute for Clinical Neurobiology were approved by the

549   Veterinäramt der Stadt Würzburg and the Committee on the Ethics of Animal Experiments

550   (Regierung von Unterfranken, Würzburg) and authorized under reference numbers 55.2-

551   2531.01-09/14; 55.2.2-2532.2-949-31.

552

553   **Primary cultures of spinal cord neurons**

554   Cultures of mixed spinal cord neurons were prepared at embryonic day 13 (E13) from

555   C57BL/6J wild-type $Glrb^{WT/WT}$ and $Glrb^{Eos/Eos}$ littermates. Spinal cord tissue was trypsinized

556   in trypsin/EDTA (1 mg/ml) and DNase I (final concentration 0.1 mg/ml) for 20 min at 37°C.

557   Trypsinization was stopped with 10% FCS. After trituration, spinal cord neurons were

558   centrifuged at 800 rpm for 10 min. Cells were plated in a 3 cm dish on polylysine-coated

559   coverslips at a density of 2-2.5 x 10^5 cells/dish. Neurons were kept at 37°C and 5% CO_2 in

560   neurobasal medium containing 2 mM L-glutamine and B27 supplement (Thermo Fisher

561   Scientific) with an exchange of half the medium after 4 days in culture.

562

563   **Electrophysiological recordings**

564   Spinal cord neuronal cultures at day *in vitro* 13 (DIV13) were used for patch-clamp

565   recordings in whole-cell configuration. Currents were amplified with a EPC-10 amplifier

566   (HEKA). A laminar flow of increasing agonist concentration (1, 10, 30, 60, 100, 300 μM

567   glycine, and 100 μM glycine/10 μM strychnine) was applied to the suspended cell using an

568   Octaflow II system (ALA Scientific Instruments), allowing 10-30 ms for equilibration. The

569   external buffer for spinal cord neurons was (in mM): 142 NaCl, 8.1 KCl, 1 $CaCl_2$, 6 $MgCl_2$,

570   10 glucose, 10 HEPES, pH adjusted to 7.4 with NaOH. To block neuronal excitability and

571   ligand-gated ion channels, the external buffer was complemented with 1 μM TTX, 10 μM

17

572 bicuculline, 10 μM CNQX, and 25 μM AP-5. The internal buffer was (in mM): 153 KCl, 1

573 MgCl$_2$, 5 EGTA, 10 HEPES, pH adjusted to 7.4 with CsOH. Recording pipettes were

574 fabricated from borosilicate capillaries with an open resistance of 4–6 MΩ. Currents were

575 measured at a holding potential of -70 mV. All experiments were performed at 22°C. The

576 mean current at each glycine concentration was determined from the peak current amplitudes

577 measured in N = 10-11 cells per genotype from three independent preparations (biological

578 replicates).

579

580 **Spinal cord and brain tissue preparation and vibratome slices**

581 Mice were sacrificed at 2 and 10 months of age by perfusion with 4% w/v paraformaldehyde

582 (PFA; Polysciences, EM grade) and 0.1% v/v glutaraldehyde (GA; Clinisciences) in

583 phosphate buffered saline (PBS, pH 7.4). Perfused animals were kept on ice for 30 min,

584 followed by the dissection of the brain and spinal cord in PBS. Tissue was post-fixed in 4%

585 w/v PFA in PBS overnight at 4 °C. Brain and spinal cord tissue was rinsed in PBS, cut into

586 smaller segments of thoracic and lumbar regions of the spinal cord and sliced on a vibratome

587 (Leica) at a thickness of 40 μm (for confocal imaging) and 300 μm (for Tokuyasu

588 preparation), and stored in PBS at 4 °C.

589

590 **Confocal imaging and analysis**

591 In order to label neuronal cells in brain slices (Fig. S3) and inhibitory synapses in *oscillator*

592 and WT littermates (Fig. 4), free-floating vibratome slices (40 μm thickness) were blocked

593 and permeabilized in PBS containing 0.25% Triton X100 (Sigma) and 0.1% fish gelatin

594 (Sigma) for 1 h, and immunolabeled with either a primary antibody against NeuN (guinea pig

595 polyclonal, 1:500 dilution, Millipore, #ABN90) or gephyrin (mouse monoclonal, mAb7a,

596 1:500 dilution, Synaptic Systems, #147011) in PBS containing 0.1% Triton X100 and 0.1%

597 fish gelatin overnight, followed by 3 hour incubation with Alexa Fluor 647-conjugated

598 secondary antibody (donkey anti guinea pig, 1:1000) or Cy3-conjugated secondary antibody

599 (goat anti mouse,1:1000, Invitrogen) respectively.

600

601 Glass slides (Vector Laboratories) were cleaned with 70% v/v ethanol (Sigma) and vibratome

602 sections were rinsed 3 times in PBS and mounted onto the glass slides. The glass slides were

603 then briefly rinsed in distilled water and dried. A drop of VectaShield (Vector Laboratories)

604 was added to each spinal cord section and covered with a #1.5 glass coverslip, which was

18

605   sealed with PicoDent Twinsil Speed (equal weights of catalyst and base). Slides were stored

606   at 4 °C for confocal imaging.

607

608   Confocal imaging was carried out on a Leica SP8 TCX microscope using a Leica HC PL

609   APO 40x/1.30 NA oil-immersion objective (Leica) and captured in 8-Bit using the Leica

610   LAS-X software with setting HyD3. Images were captured sequentially, with laser

611   illumination at wavelength 570 nm (mRFP, Cy3) imaged first, followed by laser illumination

612   at 491 nm wavelength (mEos4). A cross-section from the dorsal horn to the ventral horn was

613   imaged at a zoom of 5, speed of 25, 512 x 512 pixel (px) format. For decay analysis, 8

614   consecutive frames were captured at a zoom of 5, speed 25, 512 x 512 px format. To tile the

615   whole spinal cord, images were captured in at a zoom of 1, speed 100, 256 x 256 px format.

616

617   To ensure alignment of the clusters for the decay traces, images were opened in the image

618   analysis software ICY, and the rigid registration plug-in used, taking the first frame of mRFP-

619   gephyrin as reference. The mRFP-gephyrin/ and mEos4b-GlyRβ channels were then

620   separated and the Spot Detector plug-in (de Chaumont et al., 2012) used to identify the

621   clusters in each frame in the mRFP-gephyrin channel, with the identified clusters saved as a

622   region of interest (ROI) set. Using the image analysis software FIJI, the identified mRFP-

623   gephyrin positive cluster ROI-Set was used to identify inhibitory synapses in the first frame of

624   the mEos4b-GlyRβ channel. These inhibitory synapses were binned based on mEos4b

625   intensity gray levels (5-12, 13-24, 25-49, 50-74, 75-99, 100-124, 125-255) in frame 1 and a

626   new ROI-Set generated for each bin. Using the frame 1 intensity ROI-Sets, the integrated

627   intensity of mEos4b was then measured at individual clusters across the 8 frames. This

628   enabled decay analysis of mEos4b intensity at synapses relative to their starting intensity, see

629   Fig. 1C.

630

631   In order to analyze the intensity of mRFP-gephyrin and mEos4b-GlyRβ clusters within the

632   spinal cords from mice of different genotypes, the identified mRFP-gephyrin clusters from the

633   first frame of the decay traces (as measured by the ICY Spot Detector plug-in, see above)

634   were used to measure the relative intensity of mRFP-gephyrin and mEos4b-GlyRβ clusters at

635   those locations. The ROI-Set of all mRFP-gephyrin positive clusters was used in FIJI to

636   identify inhibitory synapses, where the integrated intensity of mRFP and mEos4b was

637   measured for each synapse (Fig. 1B).

638

639   For the cross-sectional analysis, the mRFP-gephyrin/gephyrin-7a clusters were identified

640   across the imaged tissue using the ICY Spot Detector plug-in, as described above, and saved

641   as an ROI-Set. In FIJI the integrated intensity of these identified clusters was measured in the

642   mRFP-gephyrin/gephyrin-7a channel and the mEos4b-GlyRβ channel (Fig. 1D and 1F).

643

644   **Cryosectioning of sucrose impregnated spinal cord tissue**

645   Sucrose impregnated cryosections were prepared using a ultracryotomy protocol adapted from

646   (Tokuyasu, 1973). The 300 μm spinal cord vibratome slices were transferred into a 2.3 M

647   sucrose solution in PBS overnight at 4°C and micro-dissected to isolate gray matter of the

648   dorsal and the ventral horn region. These fragments were placed individually on top of drops

649   of sucrose solution on aluminium EM pins (Leica) and immediately frozen in liquid nitrogen.

650   Sections of 2 μm thickness were sliced on an ultramicrotome (Leica EM UC6) at -80°C and

651   placed onto gridded coverslips (type 1.5 H, Ibidi GmbH), covered in PBS, and stored at 4°C

652   for a maximum of 5 days before imaging.

653

654   **Single molecule localization microscopy (SMLM)**

655   Sucrose cryosections on gridded coverslips were rinsed once in PBS, and imaged in PBS.

656   Dual-colour super resolution images were acquired on an inverted Nikon Eclipse Ti

657   microscope with a 100x/1.49 NA oil-immersion objective, with an additional 1.5x lens in the

658   emission path, using an Andor iXon EMCCD camera (16-Bit, 107 nm pixel size), and NIS-

659   Elements software (Nikon). An emission filter 607/36 was chosen for imaging both mRFP-

660   gephyrin and mEos4b-GlyRβ. Brightfield images were taken of the whole grid square

661   identifying tissue structures. Lamp images were taken of the unconverted mEos4b-GlyRβ and

662   mRFP-gephyrin (10 frames of 100 ms, ND8). mRFP-gephyrin movies of 10,000 frames were

663   recorded with HiLo 561 nm continuous laser illumination (output power 50% 400 mW, 50 ms

664   frames). This was followed by 2 min of 100% 561 nm laser illumination to ensure all mRFP-

665   gephryin was bleached. Movies of 25,000 frames were recorded with photoconversion of

666   mEos4b-GlyRβ by 0.5 ms pulsed 405 nm laser illumination (gradually increased to 100% by

667   frame 22,000) with continuous 561 nm laser illumination (output power 50% 400 mW, 50 ms

668   frames). The focal plane was maintained using a Nikon perfect focus system.

669

670

671

672

SMLM image analysis (SRRF and PALM)

673

674 Frames 100-6000 of the mRFP-gephyrin movies were taken for analysis (to remove saturated

675 frames at the beginning and bleached frames at the end) and were drift corrected and

676 reconstructed using NanoJ-SRRF plugin for FIJI (Gustafsson et al., 2016).

677 Quantification of mEos4b-GlyRβ was carried out using a lab script for MATLAB

678 (Mathworks). The mEos4b single fluorophores were detected by Gaussian fitting. The

679 resulting pointillist images were drift corrected in the x/y plane using 5 dense clusters of

680 detections over a sliding window of 2000 frames. Rendered images were produced with a

681 pixel size of 10 nm, sigma 0.01.

682

683 Fourier ring correlation (FRC) was used to estimate the spatial resolution, by dividing the odd

684 and even frames of a raw mRFP-gephyrin movie and a raw mEos4b-GlyRβ movie and

685 analyzing the resulting image stacks by SRRF and PALM, respectively. The images

686 reconstructed from the odd and even frames were then compared using the FRC tool of the

687 NanoJ-SQUIRREL plugin for FIJI (Culley et al., 2018).

688

689 The mRFP-gephyrin and mEos4b-GlyRβ rendered images were aligned by rigid registration

690 using the FIJI plug-in TurboReg. The co-localization of mRFP-gephyrin and mEos4b-GlyRβ

691 was carried out by individually cropping each synapse as separate images. The FIJI plug-in

692 Intensity correlation quotient (ICQ) was then applied to each synapse (Li et al., 2004). The

693 occupancy analysis was analyzed by thresholding the synapses in the mEos4b-GlyRβ images

694 and measuring the intensity of each synapse in both channels. To analyse the PALM mEos4b-

695 GlyRβ clusters, a lab written script for MATLAB (CountMol; (Patrizio et al., 2017)) was used

696 to identify synapses (minimum number of detections 250, minimum cluster size 200 nm,

697 maximum cluster size 3000 nm) and an intensity threshold of 0.1. For molecule conversion,

698 CountMol was used to identify extrasynaptic receptor complexes (minimum number of

699 detections 5, minimum cluster size 10 nm, maximum cluster size 120 nm). The number of

700 detections per burst (identified as a minimum of 2 detections, with 1 burst per 1000 frames)

701 and the probability of detection $P_{det} = \frac{2}{N_1/N_2+2}$ were calculated, and used to convert the

702 detections to mEos4b-GlyRβ molecules (Durisic et al., 2014, Patrizio et al., 2017), see Fig.

703 S7.

704

705

21

Electron microscopy (EM)

Cryosections used for SMLM imaging on gridded coverslips were postfixed by incubation in 1% osmium tetroxide for 1 h at 4 °C, dehydrated in graded ethanol concentrations, and embedded in araldite epoxy resin. Grid squares imaged in SMLM were identified using the grid pattern imprinted in the resin. Serial ultra-thin 70 nm sections of these regions were cut, transferred onto formvar-coated EM grids (0.432 mm slot grids) using a UC6 ultramicrotome (Leica). Sections were counterstained with 5% uranyl acetate in 70% methanol for 10 min, then washed in distilled water and air dried before observation on a Philips TECNAI 12 microscope (Thermo Fisher Scientific).

For 3D synapse reconstruction, synapses were manually outlined in each serial section image using FIJI, followed by manual rotation and coarse alignment using the software GIMP, then fine alignment of the synaptic area with the Microscopy Image Browser (MIB) software. The aligned images were then opened in IMOD software to generate the 3D reconstruction.

The length of the synaptic junction of identified synapses was measured in high magnification EM images with ImageJ software. The total area of the postsynaptic surface was calculated as the cumulative length of the postsynaptic domain in the entire stack of serial sections multiplied by the thickness of each section (70 nm). The segmentation index corresponds to the number of gaps in the postsynaptic site that were detected in the x/y plane of the images or along the z-axis (i.e. an interruption of the postsynaptic site in one or several continuous sections in the stack), and represents an estimate of the morphological complexity of the synapse.

Graphing and statistical analysis

All graphing and statistical analysis was carried out using the software GraphPad Prism v.8 for all except the electrophysiology experiments which were carried out in v.9. Data were tested for normality of distribution using D'Agostino-Pearson and Kolmogorov-Smirnov tests. Data is represented as dot plots with median ± interquartile range (IQR), or histograms, unless otherwise stated. $*p < 0.05$, $** p < 0.01$, $*** p < 0.001$, ns = not significant.

References

Alvarez FJ (2017) Gephyrin and the regulation of synaptic strength and dynamics at glycinergic inhibitory synapses. Brain Res Bull 129: 50-65

Alvarez FJ, Dewey DE, Harrington DA, Fyffe RE (1997) Cell-type specific organization of glycine receptor clusters in the mammalian spinal cord. J Comp Neurol 379: 150-70

Alvarez FJ, Taylor-Blake B, Fyffe RE, De Blas AL, Light AR (1996) Distribution of immunoreactivity for the beta 2 and beta 3 subunits of the GABAA receptor in the mammalian spinal cord. J Comp Neurol 365: 392-412

Beato M (2008) The time course of transmitter at glycinergic synapses onto motoneurons. J Neurosci 28: 7412-25

Bhumbra GS, Bannatyne BA, Watanabe M, Todd AJ, Maxwell DJ, Beato M (2014) The recurrent case for the Renshaw cell. J Neurosci 34: 12919-32

Broadhead MJ, Bonthron C, Arcinas L, Bez S, Zhu F, Goff F, Nylk J, Dholakia K, Gunn-Moore F, Grant SGN, Miles GB (2020) Nanostructural Diversity of Synapses in the Mammalian Spinal Cord. Sci Rep 10: 8189

Buckwalter MS, Cook SA, Davisson MT, White WF, Camper SA (1994) A frameshift mutation in the mouse alpha 1 glycine receptor gene (Glra1) results in progressive neurological symptoms and juvenile death. Hum Mol Genet 3: 2025-30

Chapdelaine T, Hakim V, Triller A, Ranft J, Specht CG (2021) Reciprocal stabilization of glycine receptors and gephyrin scaffold proteins at inhibitory synapses. Biophys J 120: 805-817

Chery N, de Koninck Y (1999) Junctional versus extrajunctional glycine and GABA(A) receptor-mediated IPSCs in identified lamina I neurons of the adult rat spinal cord. J Neurosci 19: 7342-55

Chow DM, Zuchowski KA, Fetcho JR (2017) In vivo measurement of glycine receptor turnover and synaptic size reveals differences between functional classes of motoneurons in zebrafish. Curr Biol 27: 1173-1183

Chung SK, Bode A, Cushion TD, Thomas RH, Hunt C, Wood SE, Pickrell WO, Drew CJ, Yamashita S, Shiang R, Leiz S, Longardt AC, Raile V, Weschke B, Puri RD, Verma IC, Harvey RJ, Ratnasinghe DD, Parker M, Rittey C et al. (2013) GLRB is the third major gene of effect in hyperekplexia. Hum Mol Genet 22: 927-40

Chung SK, Vanbellinghen JF, Mullins JG, Robinson A, Hantke J, Hammond CL, Gilbert DF, Freilinger M, Ryan M, Kruer MC, Masri A, Gurses C, Ferrie C, Harvey K, Shiang R, Christodoulou J, Andermann F, Andermann E, Thomas RH, Harvey RJ et al. (2010) Pathophysiological mechanisms of dominant and recessive GLRA1 mutations in hyperekplexia. J Neurosci 30: 9612-20

Compans B, Camus C, Kallergi E, Sposini S, Martineau M, Butler C, Kechkar A, Klaassen RV, Retailleau N, Sejnowski TJ, Smit AB, Sibarita JB, Bartol TM, Jr., Perrais D, Nikoletopoulou V, Choquet D, Hosy E (2021) NMDAR-dependent long-term depression is associated with increased short term plasticity through autophagy mediated loss of PSD-95. Nat Commun 12: 2849

Crosby KC, Gookin SE, Garcia JD, Hahm KM, Dell'Acqua ML, Smith KR (2019) Nanoscale subsynaptic domains underlie the organization of the inhibitory synapse. Cell Rep 26: 3284-3297 e3

Culley S, Albrecht D, Jacobs C, Pereira PM, Leterrier C, Mercer J, Henriques R (2018) Quantitative mapping and minimization of super-resolution optical imaging artifacts. Nat Methods 15: 263-266

de Chaumont F, Dallongeville S, Chenouard N, Herve N, Pop S, Provoost T, Meas-Yedid V, Pankajakshan P, Lecomte T, Le Montagner Y, Lagache T, Dufour A, Olivo-Marin JC (2012) Icy: an open bioimage informatics platform for extended reproducible research. Nat Methods 9: 690-6

Durisic N, Laparra-Cuervo L, Sandoval-Alvarez A, Borbely JS, Lakadamyali M (2014) Single-molecule evaluation of fluorescent protein photoactivation efficiency using an in vivo nanotemplate. Nat Methods 11: 156-62

Dzyubenko E, Rozenberg A, Hermann DM, Faissner A (2016) Colocalization of synapse marker proteins evaluated by STED-microscopy reveals patterns of neuronal synapse distribution in vitro. J Neurosci Methods 273: 149-159

Fujita M, Sato K, Sato M, Inoue T, Kozuka T, Tohyama M (1991) Regional distribution of the cells expressing glycine receptor beta subunit mRNA in the rat brain. Brain Res 560: 23-37

Goncalves J, Bartol TM, Camus C, Levet F, Menegolla AP, Sejnowski TJ, Sibarita JB, Vivaudou M, Choquet D, Hosy E (2020) Nanoscale co-organization and coactivation of AMPAR, NMDAR, and mGluR at excitatory synapses. Proc Natl Acad Sci U S A 117: 14503-14511

Gustafsson N, Culley S, Ashdown G, Owen DM, Pereira PM, Henriques R (2016) Fast live-cell conventional fluorophore nanoscopy with ImageJ through super-resolution radial fluctuations. Nat Commun 7: 12471

23

791   Haas KT, Compans B, Letellier M, Bartol TM, Grillo-Bosch D, Sejnowski TJ, Sainlos M, Choquet D, Thoumine
792   O, Hosy E (2018) Pre-post synaptic alignment through neuroligin-1 tunes synaptic transmission efficiency.
793   Elife 7

794   Harvey RJ, Depner UB, Wassle H, Ahmadi S, Heindl C, Reinold H, Smart TG, Harvey K, Schutz B, Abo-Salem
795   OM, Zimmer A, Poisbeau P, Welzl H, Wolfer DP, Betz H, Zeilhofer HU, Muller U (2004) GlyR alpha3: an
796   essential target for spinal PGE2-mediated inflammatory pain sensitization. Science 304: 884-7

797   Kim EY, Schrader N, Smolinsky B, Bedet C, Vannier C, Schwarz G, Schindelin H (2006) Deciphering the
798   structural framework of glycine receptor anchoring by gephyrin. Embo J 25: 1385-95

799   Kling C, Koch M, Saul B, Becker CM (1997) The frameshift mutation oscillator (Glra1(spd-ot)) produces a
800   complete loss of glycine receptor alpha1-polypeptide in mouse central nervous system. Neuroscience 78:
801   411-7

802   Legendre P (1998) A reluctant gating mode of glycine receptor channels determines the time course of inhibitory
803   miniature synaptic events in zebrafish hindbrain neurons. J Neurosci 18: 2856-70

804   Li Q, Lau A, Morris TJ, Guo L, Fordyce CB, Stanley EF (2004) A syntaxin 1, Galpha(o), and N-type calcium
805   channel complex at a presynaptic nerve terminal: analysis by quantitative immunocolocalization. J Neurosci
806   24: 4070-81

807   Lim R, Alvarez FJ, Walmsley B (1999) Quantal size is correlated with receptor cluster area at glycinergic
808   synapses in the rat brainstem. J Physiol 516 (Pt 2): 505-12

809   Liu YT, Tao CL, Zhang X, Xia W, Shi DQ, Qi L, Xu C, Sun R, Li XW, Lau PM, Zhou ZH, Bi GQ (2020)
810   Mesophasic organization of GABA(A) receptors in hippocampal inhibitory synapses. Nat Neurosci

811   Lorenzo LE, Godin AG, Wang F, St-Louis M, Carbonetto S, Wiseman PW, Ribeiro-da-Silva A, De Koninck Y
812   (2014) Gephyrin clusters are absent from small diameter primary afferent terminals despite the presence of
813   GABA(A) receptors. J Neurosci 34: 8300-17

814   Lu DC, Niu T, Alaynick WA (2015) Molecular and cellular development of spinal cord locomotor circuitry.
815   Front Mol Neurosci 8: 25

816   Lushnikova I, Skibo G, Muller D, Nikonenko I (2011) Excitatory synaptic activity is associated with a rapid
817   structural plasticity of inhibitory synapses on hippocampal CA1 pyramidal cells. Neuropharmacology 60:
818   757-64

819   MacGillavry Harold D, Song Y, Raghavachari S, Blanpied Thomas A (2013) Nanoscale Scaffolding Domains
820   within the Postsynaptic Density Concentrate Synaptic AMPA Receptors. Neuron 78: 615-622

821   Machado P, Rostaing P, Guigonis JM, Renner M, Dumoulin A, Samson M, Vannier C, Triller A (2011) Heat
822   shock cognate protein 70 regulates gephyrin clustering. J Neurosci 31: 3-14

823   Malosio ML, Marquèze-Pouey B, Kuhse J, Betz H (1991) Widespread expression of glycine receptor subunit
824   mRNAs in the adult and developing rat brain. Embo j 10: 2401-9

825   Maric HM, Mukherjee J, Tretter V, Moss SJ, Schindelin H (2011) Gephyrin-mediated gamma-aminobutyric acid
826   type A and glycine receptor clustering relies on a common binding site. J Biol Chem 286: 42105-14

827   Meyer G, Kirsch J, Betz H, Langosch D (1995) Identification of a gephyrin binding motif on the glycine
828   receptor beta subunit. Neuron 15: 563-72

829   Nusser Z, Cull-Candy S, Farrant M (1997) Differences in synaptic GABA(A) receptor number underlie variation
830   in GABA mini amplitude. Neuron 19: 697-709

831   Nusser Z, Lujan R, Laube G, Roberts JD, Molnar E, Somogyi P (1998) Cell type and pathway dependence of
832   synaptic AMPA receptor number and variability in the hippocampus. Neuron 21: 545-59

833   Oleskevich S, Alvarez FJ, Walmsley B (1999) Glycinergic miniature synaptic currents and receptor cluster sizes
834   differ between spinal cord interneurons. J Neurophysiol 82: 312-9

835   Patrizio A, Renner M, Pizzarelli R, Triller A, Specht CG (2017) Alpha subunit-dependent glycine receptor
836   clustering and regulation of synaptic receptor numbers. Sci Rep 7: 10899

837   Pennacchietti F, Vascon S, Nieus T, Rosillo C, Das S, Tyagarajan SK, Diaspro A, Del Bue A, Petrini EM,
838   Barberis A, Cella Zanacchi F (2017) Nanoscale molecular reorganization of the inhibitory postsynaptic
839   density is a determinant of GABAergic synaptic potentiation. J Neurosci 37: 1747-1756

840   Peters A, Palay SL (1996) The morphology of synapses. J Neurocytol 25: 687-700

841   Rudolph S, Tsai MC, von Gersdorff H, Wadiche JI (2015) The ubiquitous nature of multivesicular release.
842   Trends Neurosci 38: 428-38

843   Santuy A, Rodriguez JR, DeFelipe J, Merchan-Perez A (2018) Study of the size and shape of synapses in the
844   juvenile rat somatosensory cortex with 3D electron microscopy. eNeuro 5

Schaefer N, Langlhofer G, Kluck CJ, Villmann C (2013) Glycine receptor mouse mutants: model systems for human hyperekplexia. Br J Pharmacol 170: 933-52

Schaefer N, Roemer V, Janzen D, Villmann C (2018) Impaired glycine receptor trafficking in neurological diseases. Front Mol Neurosci 11: 291

Schaefer N, Vogel N, Villmann C (2012) Glycine receptor mutants of the mouse: what are possible routes of inhibitory compensation? Front Mol Neurosci 5: 98

Singer JH, Berger AJ (1999) Contribution of single-channel properties to the time course and amplitude variance of quantal glycine currents recorded in rat motoneurons. J Neurophysiol 81: 1608-16

Specht CG (2020) Fractional occupancy of synaptic binding sites and the molecular plasticity of inhibitory synapses. Neuropharmacology 169: 107493

Specht CG, Izeddin I, Rodriguez PC, El Beheiry M, Rostaing P, Darzacq X, Dahan M, Triller A (2013) Quantitative nanoscopy of inhibitory synapses: counting gephyrin molecules and receptor binding sites. Neuron 79: 308-21

Takahashi T (1992) The minimal inhibitory synaptic currents evoked in neonatal rat motoneurones. J Physiol 450: 593-611

Tang AH, Chen H, Li TP, Metzbower SR, MacGillavry HD, Blanpied TA (2016) A trans-synaptic nanocolumn aligns neurotransmitter release to receptors. Nature 536: 210-4

Todd AJ, Watt C, Spike RC, Sieghart W (1996) Colocalization of GABA, glycine, and their receptors at synapses in the rat spinal cord. J Neurosci 16: 974-82

Tokuyasu KT (1973) A technique for ultracryotomy of cell suspensions and tissues. J Cell Biol 57: 551-65

Weltzien F, Puller C, O'Sullivan GA, Paarmann I, Betz H (2012) Distribution of the glycine receptor beta-subunit in the mouse CNS as revealed by a novel monoclonal antibody. J Comp Neurol 520: 3962-81

Yang X, Le Corronc H, Legendre P, Triller A, Specht CG (2021) Differential regulation of glycinergic and GABAergic nanocolumns at mixed inhibitory synapses. EMBO Rep 22: e52154

Yang X, Specht CG (2019) Subsynaptic domains in super-resolution microscopy: The treachery of images. Front Mol Neurosci 12: 161

Zeilhofer HU, Studler B, Arabadzisz D, Schweizer C, Ahmadi S, Layh B, Bosl MR, Fritschy JM (2005) Glycinergic neurons expressing enhanced green fluorescent protein in bacterial artificial chromosome transgenic mice. J Comp Neurol 482: 123-41

Figures and Legends
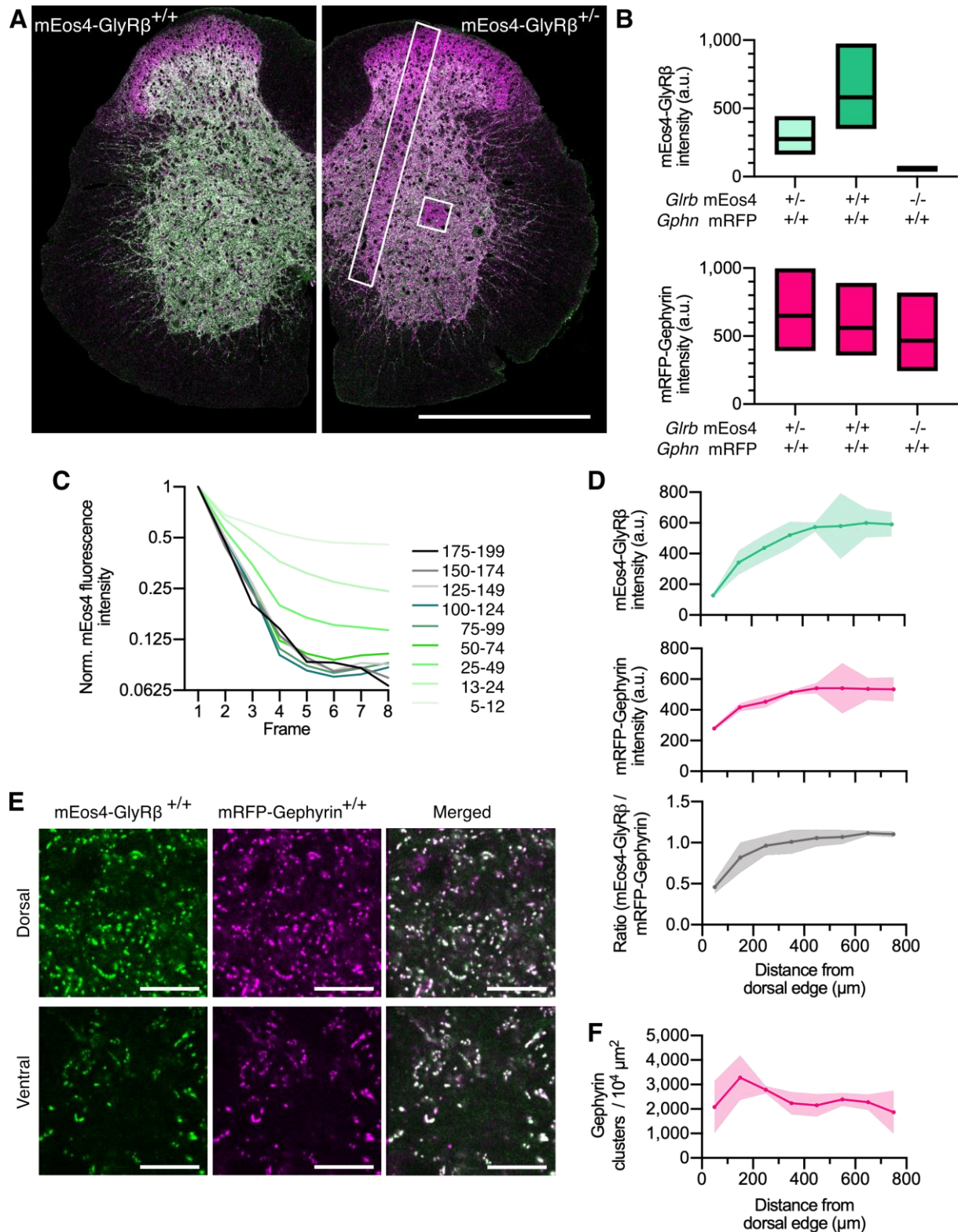
Fig. 1. **Quantitative confocal imaging of endogenous GlyRs in spinal cord tissue.** (A) Representative confocal images of 40 μm spinal cord tissue sections from homozygous (+/+) and heterozygous (+/-) mEos4b-GlyRβ mice (green). Both mice are homozygous for mRFP-gephyrin (magenta). Scale bar = 0.5 mm. (B) Quantification of mEos4b-GlyRβ and mRFP-gephyrin fluorescent intensity of homozygous and heterozygous 2 month old animals

885   measured in the area indicated by the white square in (A). Plots show median and quartiles. N

886   = 5-6 images from 5-6 tissue slices per genotype from 2 mice per age group. (C) Normalized

887   fluorescent decay traces of homozygous mEos4b measured in the area indicated by the white

888   square in (A) over 8 consecutive frames. Intensities were binned in the first image and tracked

889   on an individual synapse basis across the 8 frames. (D) Mean intensity ± 95% confidence

890   interval of mEos4b-GlyRβ and mRFP-gephyrin measured from distal edge of spinal cord in 2

891   month old homozygous mice. Intensities measured in region as indicated by white rectangle

892   in (A). N = 3 images from 3 tissue slices from 2 mice per condition. (E) Representative

893   images of homozygous mEos4b-GlyRβ and mRFP-gephyrin at dorsal and ventral synapses.

894   Scale bar = 10 μm. (F) Quantification of numbers of gephyrin clusters across the spinal cord.

895   Plot shows mean ± 95% confidence interval. N = 3 images from 3 tissue slices from 2 mice

896   per condition.

897
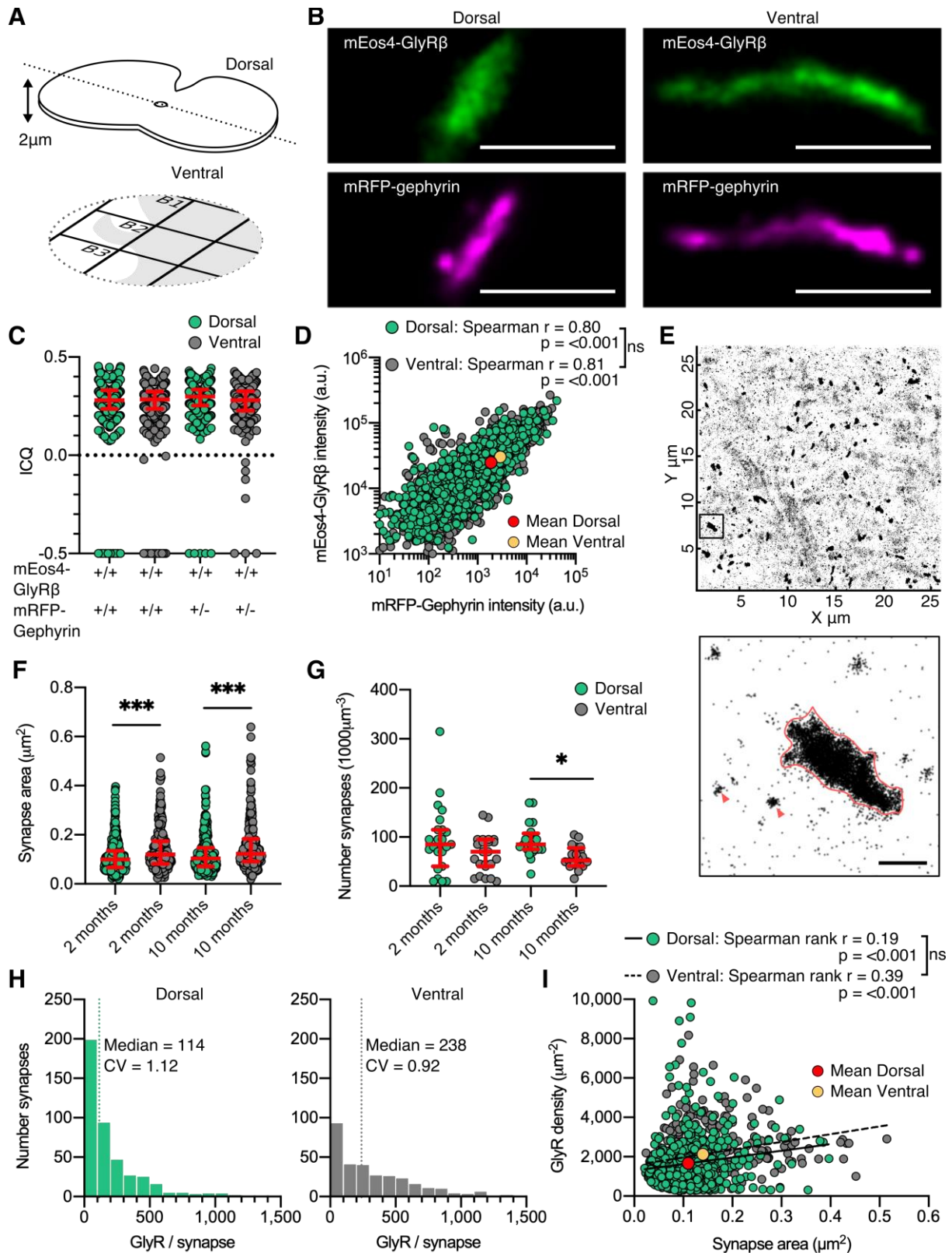
Fig. 2. Dual-color super-resolution imaging of mEos4b-GlyRβ and mRFP-gephyrin. (A) 2 μm cryosections of spinal cord tissue were cut from dorsal and ventral tissue and placed on gridded glass coverslips. (B) Representative PALM reconstruction of mEos4b-GlyRβ and SRRF reconstruction of mRFP-gephyrin at single dorsal and ventral synapses. Scale bar = 500 nm. (C) Intensity correlation quotient (ICQ) of mEos4b-GlyRβ and mRFP-gephyrin in

28

905   heterozygous and homozygous 2 month old mice. Plot shows median ± interquartile range. N
906   = 357-604 synapses from 23 dorsal and 23 ventral images from 9 and 8 tissue slices
907   respectively from 2 mice per condition. (D) Quantification of GlyR-gephyrin occupancy in 2
908   month old homozygous mice ($Glrb^{Eos/Eos}$ / $Gphn^{mRFP/mRFP}$). Non-parametric Spearman's rank
909   shows the same positive correlation at dorsal and ventral synapses. N = 1115 dorsal synapses
910   and 1107 ventral synapses. (E) Pointillist reconstruction of mEos4b-GlyRβ detections. Insert
911   shows a single synapse; red arrows indicate extrasynaptic receptor complexes. Scale bar =
912   500 nm. (F) Area of dorsal vs ventral synapses in 2 and 10 month old homozygous mice. Plot
913   shows median ± interquartile range. N = 234-433 synapses from 20-23 images from 7-9 tissue
914   slices from 2 mice per age per condition. Nonparametric Kruskal-Wallis ANOVA with
915   Dunn's multiple comparison test. (G) Number of synapses in dorsal and ventral tissue in 2
916   and 10 month old homozygous mice. Plot shows median ± interquartile range. N = 20-23
917   images from 7-9 tissue slices from 2 mice per age per condition. Nonparametric Kruskal-
918   Wallis ANOVA with Dunn's multiple comparison test. (H) Histogram of the number of
919   GlyRs per synapse calculated from the molecular conversion of detections (see Fig. S6 and
920   S7) in 2 month old homozygous mice. N = 433 dorsal synapses and 304 ventral synapses
921   from 23 dorsal and 23 ventral images from 9 and 8 tissue slices respectively from 2 mice. CV
922   = coefficient of variation. (I) Scatter plot of GlyR density vs synapse area in 2 month old
923   homozygous mice shows no difference between dorsal and ventral synapse densities. N = 433
924   dorsal synapses and 304 ventral synapses. *p < 0.05, **p < 0.01, ***p < 0.001.
925
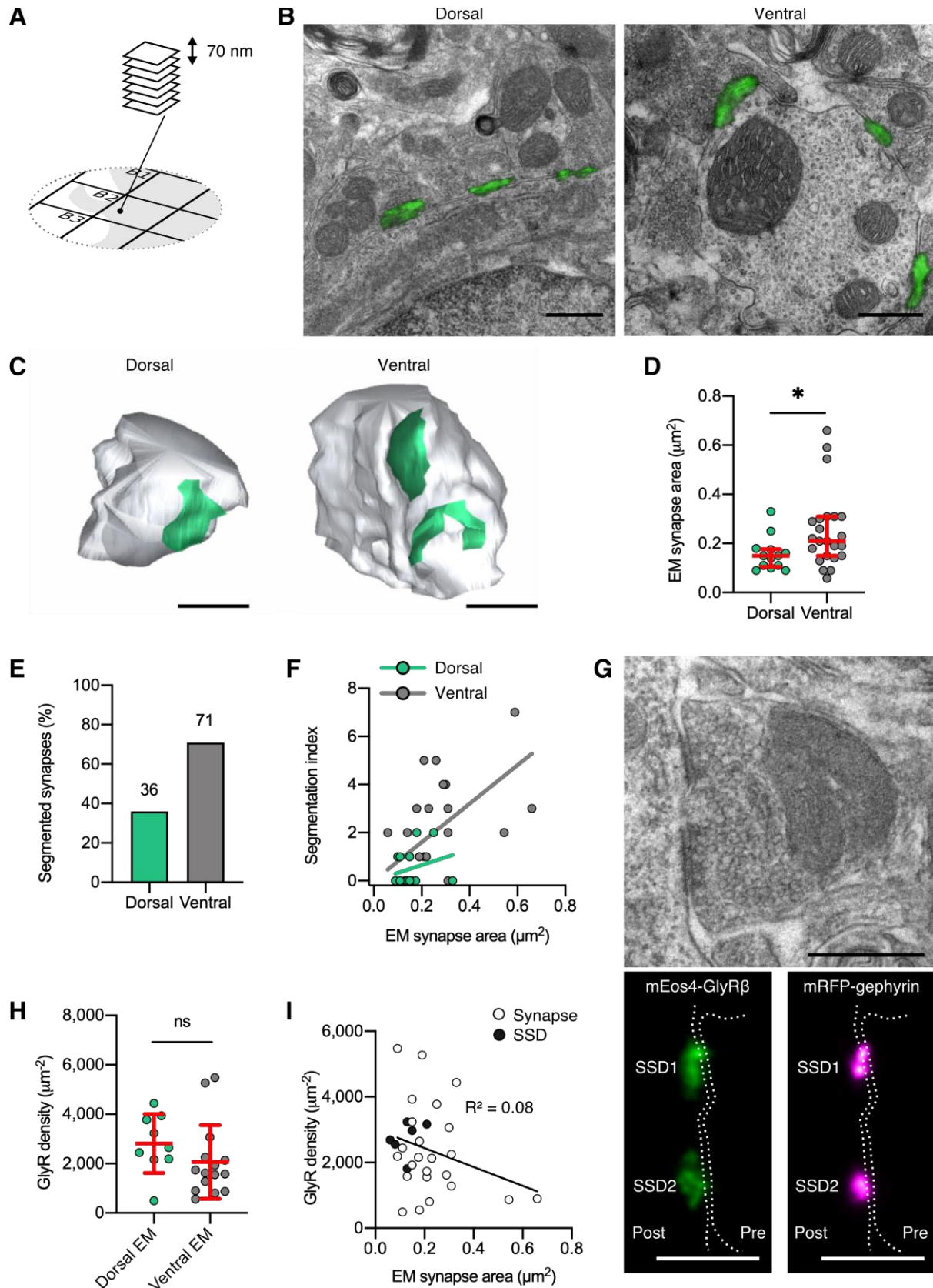
Fig. 3. Quantitative SR-CLEM of endogenous GlyR molecular organization. (A) Samples used for PALM were re-sectioned as serial ultra-thin 70 nm sections for CLEM. (B) Representative dorsal and ventral synapses imaged with PALM (mEos4b-GlyRβ; green) and super-imposed with their corresponding electron micrographs. Scale bar = 500 nm. (C)

932   Representative 3D reconstructions of dorsal and ventral synapses. Green = postsynaptic site,
933   gray = presynaptic bouton. Scale bar = 500 nm. (D) Area of dorsal and ventral synapses
934   measured by EM. Plot shows median ± interquartile range. Nonparametric unpaired two-
935   tailed t-test, Mann-Whitney post hoc. (E) Percentage of total synapses measured in EM with
936   segmented shapes. (F) Comparison of segmentation index with synaptic area in dorsal and
937   ventral synapses. (G) Juxtaposition of a raw electron micrograph and reconstructed
938   PALM/SRRF images of sub-synaptic domains (SSDs) in the same ventral synapse. Scale bar
939   = 500 nm. (H) Analysis of GlyR density following correction for EM area measurements. Plot
940   shows mean ± SD. (I) Combined scatter plot of dorsal and ventral synapse densities shows
941   density is independent of synapse size. White = all synapses, black = SSDs. N = 13 dorsal and
942   23 ventral synapses from 2 mice. *p < 0.05, ns = not significant.
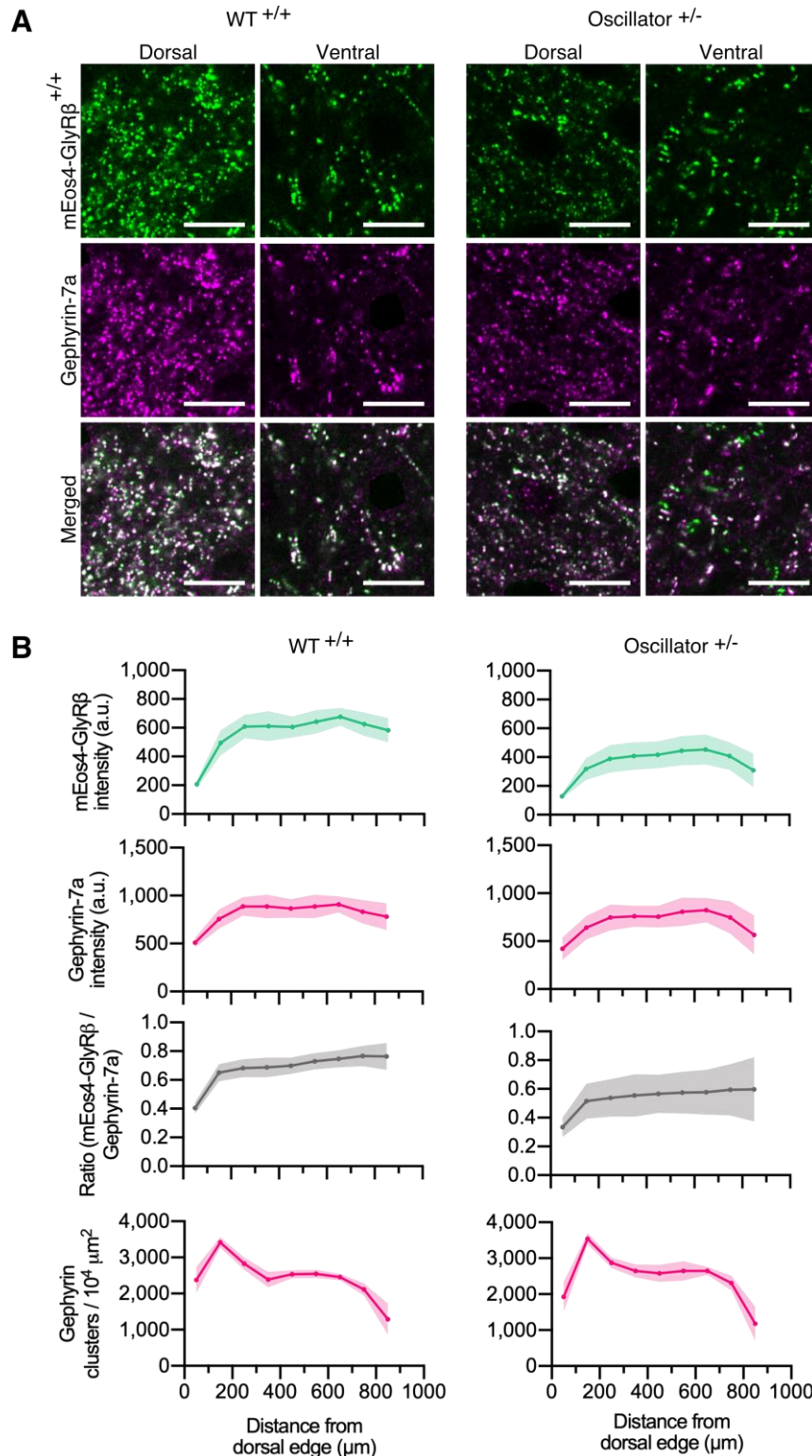
Fig. 4. Quantitative confocal imaging of endogenous GlyRs in the *oscillator* mouse model. (A) Representative confocal images of dorsal and ventral synapses from heterozygous *oscillator* mice (+/-) compared to homozygous WT (+/+) littermates. All mice are homozygous for mEos4b-GlyRβ (green), with gephyrin-7a immunolabeling (magenta). Scale bar = 10 μm. (B) Mean intensity ± 95% confidence interval of mEos4b-GlyRβ and gephyrin-7a at gephyrin-positive puncta, and numbers of gephyrin clusters measured from distal edge of spinal cord in 2 month old mice. N = 9-11 images from 9-11 tissue slices from 2 mice per genotype.
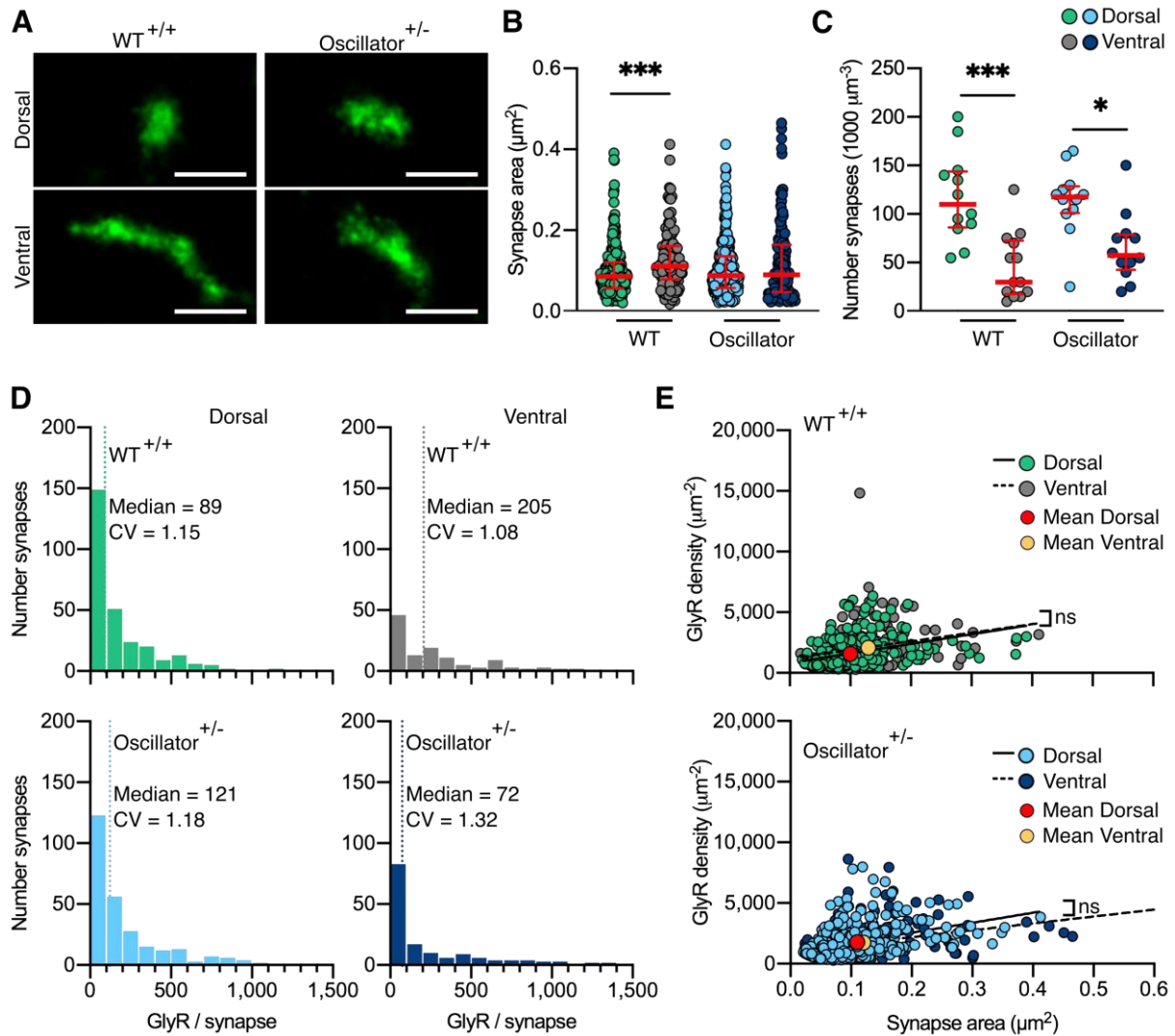
Fig. 5. PALM imaging of the GlyR in the *oscillator* mouse model. (A) Representative PALM reconstructions of mEos4b-GlyRβ at single dorsal and ventral synapses in heterozygous (+/-) *oscillator* and homozygous (+/+) WT littermates. All mice are homozygous for mEos4b-GlyRβ. Scale bar = 500 nm. (B) Area of dorsal vs ventral synapses in heterozygous *oscillator* vs WT littermates. Plot shows median ± interquartile range. N = 120-282 synapses from 24 images from 9-11 tissue slices from 2 mice per genotype. Nonparametric Kruskal Wallis ANOVA with Dunn's multiple comparison test. (C) Number of synapses in dorsal and ventral tissue in heterozygous *oscillator* vs WT mice. Plot shows median ± interquartile range. N = 12-13 images from 2 mice per genotype. Parametric one-way ANOVA with Tukey's multiple comparison test. (D) Histogram of the number of GlyRs per synapse calculated from the molecular conversion of detections (see Fig. S7, S11 and S12). N = 282 WT dorsal and 120 ventral synapses, 273 *oscillator* dorsal and 156 ventral synapses from 24 images from 9-11 tissue slices from 2 mice per genotype. CV = coefficient of variation. (E) Scatter plots of GlyR density vs synapse area show no difference between dorsal and ventral synapse densities in WT and *oscillator*. N = same as in (D). *$p < 0.05$, ***$p < 0.001$, ns = not significant.

33